Spin-orbital coupling induced isolated flat band in bismuthene with k-dependent spin texture

Shifang Li [1,2] Xizhi Shi,[1,2] Jin Li [1,2,*] Chaoyu He [1,2,†] Tao Ouyang,[1,2] Chao Tang,[1,2] and Jianxin Zhong[3,2]

[1]*School of Physics and Optoelectronics, Xiangtan University, Xiangtan 411105, China*
[2]*Hunan Key Provincial Laboratory of Micro-nano Energy Materials and Devices, Xiangtan University, Hunan 411105, China*
[3]*Center for Quantum Science and Technology, Shanghai University, Shanghai 200444, China*

Flat bands exhibit many exotic physical phenomena due to the dispersionless features and are receiving widespread attentions. In this work, a metastable bismuthene allotrope (*P-3m1*-Bi$_{72}$) with isolated flat bands near the Fermi level was identified, through high-throughput tight-binding calculations, from more than 500 allotropes. *P-3m1*-Bi$_{72}$ features the kagome characteristic of an interlaced distribution of triangles and hexagons. First-principles calculations revealed that this structure is a dynamically stable phase of bismuthene and energetically more favorable than many previously predicted bismuthene allotropes. Based on the high-level functional of HSE06 (HSE stands for Heyd-Scuseria-Ernzerhof), three isolated flat bands are confirmed in the band structures of *P-3m1*-Bi$_{72}$, located in the vicinity of the Fermi level. These isolated flat bands originate from the kagome-like features of the atomic configuration as well as the charge distributions, and their isolation and flatness are severely affected by the strength of spin-orbital coupling (SOC). Additionally, the spin textures of flat bands in *P-3m1*-Bi$_{72}$ are **k** dependent and exhibit twofold rotation symmetry in reciprocal space. Our work provides a candidate material for studying the properties of isolated flat bands in a strong SOC system.

I. INTRODUCTION

Flat band means a special band structure exhibiting a dispersionless feature that the energy bands $E(k)$ are almost independent of momentum k. When the kinetic energy is quenched, the interaction energy becomes crucial throughout the entire Hamiltonian, making the flat-band systems exhibit strong correlation effects [1,2]. Flat-band systems are ideal platforms for realizing the fascinating physical phenomena [3,4] of superconductivity [5–7], Wigner crystallization [8,9], anomalous quantum Hall effect [10], supersolidity [11], and dipolar interaction magnets [12]. The confirmation of magic-angle graphene bilayers as a flat-band system [13] has sparked a new wave of exploring two-dimensional flat-band materials. Usually, flat bands can be constructed by topological defects [14,15] or designed in special lattice models with compact localized state, such as kagome [16] and Lieb [17]. However, flat bands in real materials typically experience disturbances leading to a certain degree of dispersion. They often deviate from the Fermi level or overlap with dispersive bands. The isolated zero-energy flat bands are highly expected in condensed-matter physics in view of their advantages in many practical applications by avoiding the influence of other factors [18].

Spin-orbit coupling (SOC) is an intrinsic interaction in physics that describes how the spin of particles interacts with their orbital motion, which largely influences the electronic structure of materials. Most of the previously reported flat-band systems are light-element materials with weak SOC [2,9,13,14]. Designing flat-band systems based on strong SOC materials is an intriguing topic, but presently there is relatively little research on this subject. Flat-band systems with strong SOC are highly expected to extend their functionalities for applications in spintronics [19,20], and they have recently garnered significant research interest [21]. For example, Hiroki *et al.* have demonstrated that SOC-related flat bands can be realized in pyrochlore and kagome lattices [22]. Especially, SOC can open a small band gap and isolate the flat band from the dispersion band [23], and some SOC-related quasi-flat-bands [24] have been experimentally confirmed, such as CoSn [25]. Unlike ordinary flat bands, electrons in SOC-related flat bands interfere destructively through spin selection rules controlled by $SU(2)$ gauge fields [26], resulting in localized charge distributions in real space [22]. Therefore, flat-band systems in strong SOC materials are more worthy of expectation in condensed-matter physics.

Bismuth, as the heaviest element in the group 15, possesses strong SOC. Previous studies have suggested that bismuth can form various allotropes [27–30] due to its 3-coordinated bonding features. Furthermore, the air stability of bismuth surpasses that of phosphorus and arsenic [31], which is crucial for practical applications [32]. It is believed that bismuth can provide a large number of allotropes with different electronic properties, such as the SOC-related flat band. In fact, some 2D bismuth allotropes have been experimentally synthesized, such as Bi(111) and Bi(110) thin films [33,34]. Their outstanding spintronic properties enable the conversion between spin and charge currents in future integrated circuits [35,36], making them candidate materials for spintronics [37]. The prediction of Bi(110) thin film as an elementary ferroelectric

---

*Contact author: lijin@xtu.edu.cn
†Contact author: hechaoyu@xtu.edu.cn

115115-1
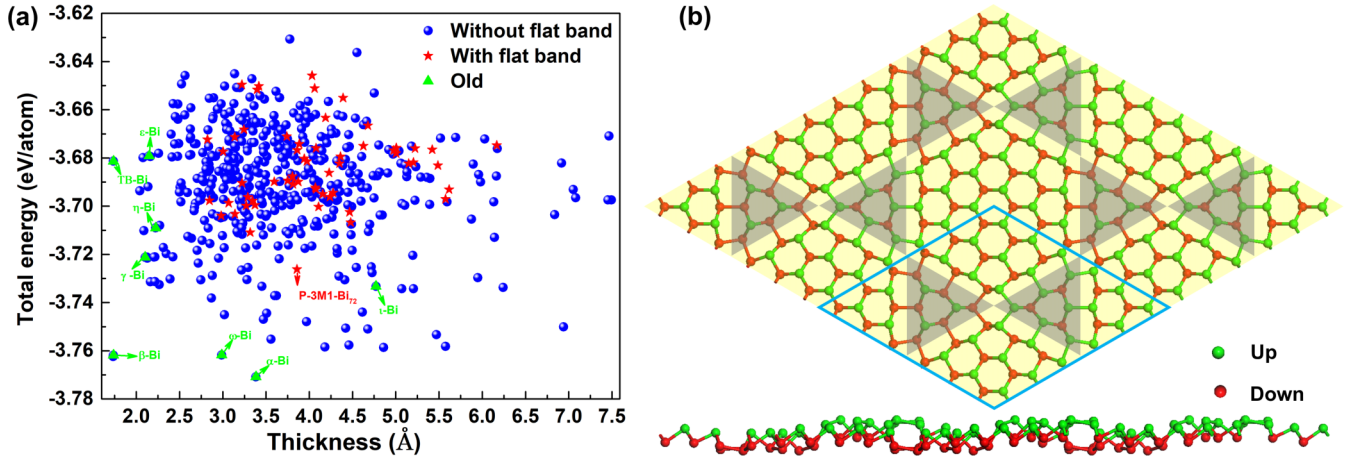
FIG. 1. (a) Total energy and structure thickness relationship for 8 old structures (green triangles), 57 bismuth structures with flat bands (red pentagrams), and 467 structures without flat bands (blue solid circles). (b) Top and side views of the optimized P-$3m1$-Bi_{72} structure, with cyan diamond representing the primitive cell.

material [38] has been recently confirmed [39] by experiment, which has attracted further research interests in 2D bismuth systems [40–43]. Here, we are highly curious about whether it is possible to design flat-band materials in 2D bismuth allotropes.

With the development of advanced preparation methods for two-dimensional materials, the potential diversity of bismuthene is promising under suitable substrates and growth conditions. Presently, common theoretical phosphorene and bismuthene isomers are viewed as different undulating hexagonal lattices. This inspires the theoretical design of more bismuthene allotropes through the random undulation of hexagonal lattice supercells. In this study, a high-throughput approach combining the random method with group theory and graph theory (RG^2) [44–46], first-principles calculations, Vienna *Ab initio* Simulated Package (VASP) [47], and the tight-binding (TB) approximation [48,49] is employed to investigate the atomic structures and electronic properties of potential bismuthene allotropes. Based on the quotient graphcoloring strategy in RG^2, hundreds of possible undulated configurations have been generated as potential bismuthene isomers. Interestingly, there are indeed some configurations that exhibit flat bands, including a low-energy one (P-$3m1$-Bi_{72}) with three isolated flat bands near the Fermi level. It is further confirmed to be dynamically stable based on first-principles calculations. Comparative studies indicate that these isolated flat bands with SOC-dependent isolation and flatness originate from the kagome-like feature of atomic configuration and charge distributions. Furthermore, the spin textures of the flat bands in such a 2D bismuth system are **k** dependent and show twofold rotation symmetry in reciprocal space. Our work provides a candidate material for studying the properties of isolated flat bands in systems with strong SOC.

II. COMPUTATION DETAILS

To find sufficient configurations with corrugated and 3-connected features for 2D bismuth allotrope, the planar honeycomb lattice in different hexagonal and rectangular supercells is considered as starting points. Corrugations can be simply constructed by creating different up (U) and down (D) atomic positions of bismuth in the supercells. This can be efficiently finished by our previously developed RG^2 [44,45,50]. Although the 2D materials we study can be described by layer groups, they need to be treated as three-dimensional (3D) crystals to be recognized by commonly used first-principles calculation software and crystal-structure editing tools. Therefore, in our research, we select a third lattice vector perpendicular to the *a-b* plane and choose to label them using 3D space groups. In our present work, only small-size cells with a total atom number smaller than 80 are considered. The configurations with neighborhood relationships of U:UUU and D:DDD are directly dropped by RG^2 due to their potentially higher energy. Finally, 524 surviving candidates are selected for further investigations of their structures, stabilities, and electronic properties based on the widely used VASP [47]. As the total energies summarized in Fig. 1(a) as a function of layer thickness, many corrugated candidates of 2D bismuth with remarkable energetic stabilities are discovered. Some of these discovered candidates are energetically more favorable than most of the previously proposed ones, such as TB-Bi [51], ε-Bi and η-Bi [27,52]. The experimentally synthesized α-Bi [53] is obviously the ground state of 2D bismuth with the lowest total energy.

To gain accurate results of electronic band structures, the high-level hybrid functional of HSE06 (HSE stands for Heyd-Scuseria-Ernzerhof) [54] is expected. However, it is time-consuming and too expensive for high-throughput calculations. To address this issue, a general and transferable TB model based on sp^3d^5 orbitals of Bi allotropes is considered, and the details of such a TB model can be found in our previous work [48,49,55,56]. The HSE06-based band structures of three old structures of MBi, β-Bi, and α-Bi with and without SOC are selected to fit the TB parameters for 2D bismuth allotropes. In order to enhance the universality of the TB model, the fitting cutoff radius is expanded to 15 Å. The final optimized TB parameters are shown in Supplemental Material, Table S1 [57], and the corresponding band structures of the three selected old allotropes are shown in Fig. S1 [57]. It can be seen that the electronic properties calculated by the

TB model are consistent with the HSE06-based ones very well. It is worth mentioning that these three selected structures have different geometric configurations and electronic properties, including rectangular, hexagonal, and square unit cells with atomic layer thickness ranging from 1.6 to 3.5 Å, as well as metal, semiconductor, and semimetal. Furthermore, the transferability of our optimized TB parameters can be further confirmed by the band structures of three additional 2D bismuth structures of TB-Bi, ω-Bi, and ε-Bi, as shown in Fig. S2 [57]. These results indicate that our TB parameters have strong universality and can be applied to calculate other 2D bismuth allotropes.

III. RESULTS AND DISCUSSION

Based on the optimized TB parameters, the electronic band structures of all the 524 2D bismuthene allotropes with and without SOC are rapidly calculated. It is found that most of them are semiconductors. To identify the flat bands in these systems, we set the criterion for bandwidth to be 30 meV. Since people are only concerned with the energy bands near the Fermi level, we have evaluated only the ten bands above and below the Fermi level. Finally, 57 configurations have been confirmed as flat-band systems under the width criterion of 30 meV. The configurations with and without flat bands are denoted in Fig. 1(a) as red pentagram and blue solid circles, respectively. It can be seen that the proportion (10.9%) of flat bands in 2D bismuthene is very small. The band structures of the 57 flat-band systems are shown in Figs. S3 and S4 [57], in which the flat bands are denoted as red solid lines. Their optimized crystal structures are provided in a res.format file in the Supplemental Material for interested researchers [57].

As shown in Fig. 1(a), the one with the lowest total energy among all the flat-band systems attracted our interest. It contains 72 bismuth atoms in its hexagonal cell in *P-3m1* (164) symmetry and can be correspondingly named as *P-3m1*-Bi$_{72}$. The optimized crystal structure of *P-3m1*-Bi$_{72}$ is shown in Fig. 1(b), where the green and red balls represent the upward and downward Bi atoms, respectively. Its optimized lattice constants are $a = b = 25.48$ Å and $c = 22.19$ Å. There are two different segments of hexagon and triangle separated by an obvious kagome-type boundary. All the Bi atoms in each hexagon and triangle are alternating upward and downward similar to those atoms in the β-Bi [28] and blue phosphorene [58]. It is clearly seen that there are 9 pairs of (upward or downward) Bi–Bi bonds surrounding each triangle segment, and the hexagon is enclosed by 18 pairs of Bi–Bi bonds (alternating upward and downward). In *P-3m1*-Bi$_{72}$, all Bi atoms are 3-coordinated with bond lengths ranging from $3.030 \sim 3.098$ Å and bond angles range from $73.96° \sim 107.81°$. These bond characters are similar to those in β-Bi [28], but the layer thickness of *P-3m1*-Bi$_{72}$ of 3.88 Å is twice larger than that of β-Bi (1.74 Å).

The average energy of *P-3m1*-Bi$_{72}$ is -3.726 eV per atom, which is higher than the experimentally synthesized allotropes β-Bi (-3.762 eV per atom) [33] and α-Bi (-3.771 eV per atom) [53]. It should be noticed that such energy is lower than that of the experimentally observed Mbi [34] (-3.579 eV per atom), which indicates that the discovered *P-3m1*-Bi$_{72}$ is expectable. The thermal stability of *P-3m1*-Bi$_{72}$ is also confirmed by the *ab initio* molecular dynamics at 300 K. As shown in Fig. S5(a) [57], the total energy just slightly oscillates around the equilibrium energy and the final structure remains intact after a 5-ps simulation. We have also calculated the vibrational spectrum of *P-3m1*-Bi$_{72}$ to evaluate its dynamical stability. The results in Fig. S5(b) show that no negative frequency appears in the phonon-band spectrum [57]. Furthermore, the phonon density in the whole first Brillouin zone (BZ) also contains no imaginary vibrational modes, which further confirms that *P-3m1*-Bi$_{72}$ is dynamically stable under small vibrations. Based on its thermal and dynamic stability, as well as relatively lower total energy, *P-3m1*-Bi$_{72}$ is expected to be realized in future experiments.

The electronic band structures of *P-3m1*-Bi$_{72}$ with and without SOC in TB are shown in Figs. 2(a) and 2(b), respectively. It can be seen that without SOC, the system exhibits the properties of a normal indirect band-gap semiconductor with a gap of 1101 meV. With included SOC effect, the system is still an indirect band-gap semiconductor with a reduced band gap of 396.6 meV. However, there are three isolated flat bands near the Fermi level. To confirm these electronic band features of *P-3m1*-Bi$_{72}$, the hybrid functional HSE06 is employed to calculate the band structures again and the results are in good consistence with those deduced by our TB calculations as shown in Fig. 2. The isolated flat bands near the Fermi level are denoted by VB1, CB1, and CB3 in Fig. 2(b) and their bandwidths are calculated to be 105.84, 19.8, and 26.1 meV, respectively. These bandwidths are much smaller than the criterion of 50 meV used for selecting flat bands in previous works [59] and comparable to the flat-band width (12 meV) in twisted bilayer magic graphene [13]. Especially, valence band 1 (VB1), conduction band 1 (CB1), and CB3 have much smaller dispersion in the *M-K* path, where the corresponding bandwidth is only 1.03, 2.84, and 1.07 meV, respectively. These values are much smaller than the width of the flat band in the twisted bilayer magic graphene. The maximum Fermi velocities of VB1, CB1, and CB3 are calculated to be 16.5×10^4, 4.43×10^4, and 5.33×10^4 m/s, respectively, which are close to that of twisted bilayer graphene in magic angle (4×10^4 m/s) [13]. For VB1 and CB1 along *M-K*, the maximum Fermi velocities are about one order of magnitude smaller, which are only 0.503×10^4 and 0.902×10^4 m/s. From the HSE06-based density of states as plotted in Fig. 2(b) (green solid line), it can be seen that there are corresponding sharp peaks appearing for reflecting the flat bands. To visualize the characteristics of the isolated flat bands, the high-level HSE06 is employed to calculate the 3D band structure of *P-3m1*-Bi$_{72}$ in the hexagonal BZ. Like the results displayed in Fig. 2(c), CB1 and CB3 are nearly flat throughout the entire BZ, which is consistent with our conclusions drawn from the 2D band-structure analysis.

For the band structure without SOC, it is known that in the planar kagome structure, both a flat band and a Dirac cone composed of p_z orbitals appear simultaneously [9,12]. However, the *P-3m1*-Bi$_{72}$ does not exhibit obvious flat bands without SOC, as depicted in Fig. 2(a). This may be attributed to structural fluctuations and strong hybridization between the p_z and other orbitals, resulting in the absence of flat bands solely composed of p_z orbitals. Intriguingly, multiple isolated flat bands can be induced in *P-3m1*-Bi$_{72}$ when SOC is
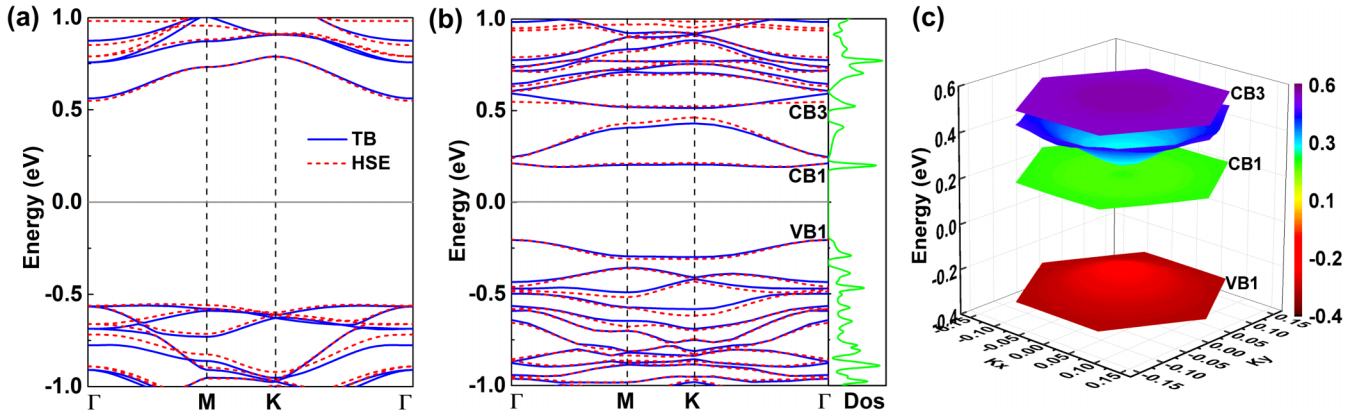
FIG. 2. The band structures of P-$3m1$-Bi$_{72}$ calculated with density-functional theory (DFT)-HSE06 (red dashed line) and TB (blue solid line) without SOC (a) and with SOC (b); (c) The 3D band structure of P-$3m1$-Bi$_{72}$ calculated by HSE06 with SOC. The high-symmetry points Γ, M, K are defined in Fig. 4(d).

included. To further explore the effect of SOC on the electronic properties of P-$3m1$-Bi$_{72}$, we calculate its band structure based on the TB method with considering different SOC strength (λ) as included as $H_\lambda = \lambda L \cdot S$, where L and S represent orbital angular momentum and electron spin, respectively. The band structure with $\lambda = 1/3$ is shown in Fig. S6(b) [57], where the highest and second valence bands are separated at point Γ. Additionally, the band gap between

the highest valence band and the lowest conduction band decreases. With increased λ of 2/3, the highest valence band and the lowest conduction band become more flat, and the highest valence band is isolated, as shown in Fig. S6(c) [57]. As shown in Fig. S6(d) [57], three isolated flat bands (VB1, CB1, and CB3) are obtained at $\lambda = 1$, and the band gap decreases to 396.6 meV. That is to say, the highest valence band will be isolated and become more and more flat with the increase of
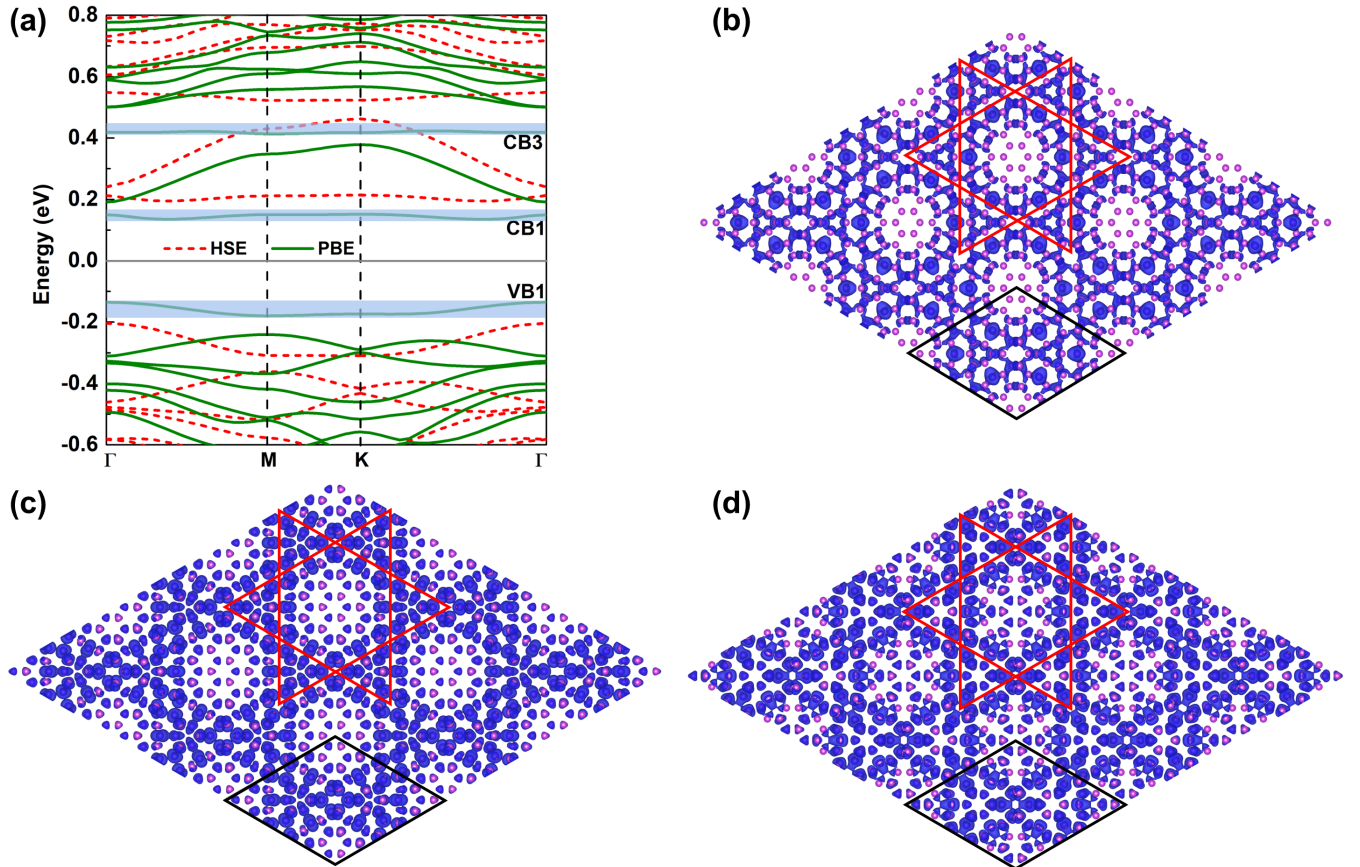
FIG. 3. (a) Band structures of P-$3m1$-Bi$_{72}$ calculated using HSE and PBE, with three blue regions indicating the energy ranges of the VB1, CB1, and CB3 flat bands. (b)–(d) Charge distributions near the VB1, CB1, and CB3 flat bands, respectively, in a 3 × 3 supercell, with black diamonds representing the primitive cell and red hexagonal stars used as guides for the eyes.
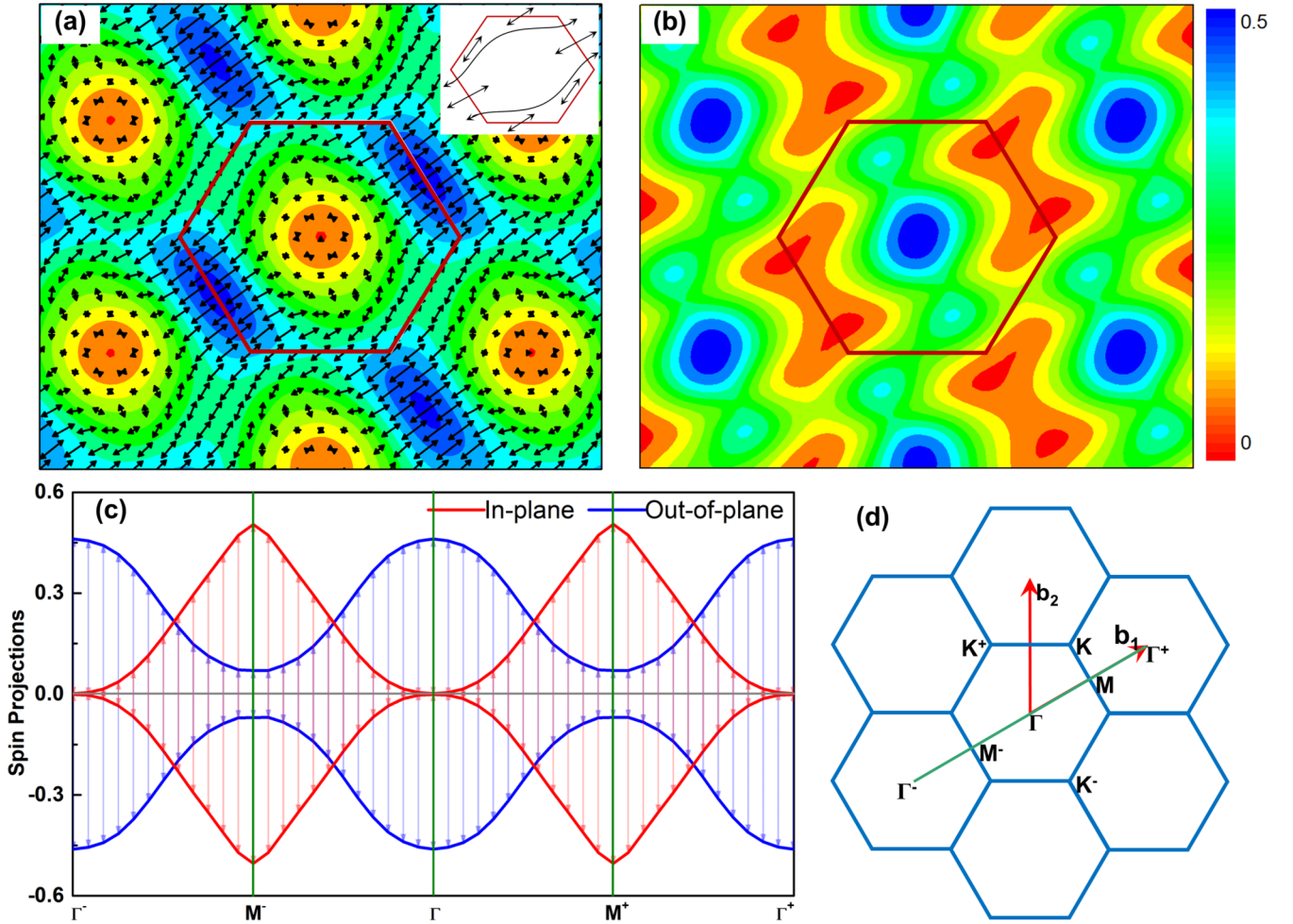
FIG. 4. Spin textures of the highest valence band: (a) and (b) represent the projection of the in-plane and out-of-plane spin magnitudes in reciprocal space, respectively, where the black arrows represent the in-plane spin textures and the blue and red colors represent the spin magnitudes, with more blue indicating a larger spin. (c) Spin magnitudes along the Γ-M direction. (d) The Brillouin zone, with red arrows representing reciprocal lattice vectors and orange lines indicating the extension line of the Γ-M direction.

SOC, while with increased SOC, the lowest conduction band will be finally identified as a flat band and the band gap of the system will gradually decrease. This phenomenon reflects that strong SOC of the bismuth element plays an important role in the formation of the isolated flat bands in P-$3m1$-Bi_{72}.

To further understand the origin of the flat bands, we have studied the spatial distributions of the charge density of the VB1, CB1, and CB3 bands. The band structure of P-$3m1$-Bi_{72} calculated by PBE (Perdew, Burke, and Ernzerhof) and HSE06 is shown in Fig. 3(a); it is found that the PBE (green solid line) calculation underestimates its band gap in comparison with HSE06 (red dashed line). Fortunately, the PBE calculation can also describe the isolated flat bands very well. Thus, the low-cost PBE method is adopted to calculate the charge density of the flat bands in our present work. As shown in Figs. 3(b), 3(c), and 3(d), the PBE-based spatial charge densities for different isolated flat bands are illustrated. It is obvious that the charge distribution of VB1 [Fig. 3(b)] is concentrated nearby the kagome boundaries, while there is almost no charge distribution in the interior of hexagons and triangles. The charge distributions of CB1 and CB3, as shown in Figs. 3(c) and 3(d), also look very much like

kagome patterns. These distributions of charge densities are in good agreement with the fact that P-$3m1$-Bi_{72} is formed by a kagome-type boundary consisting of hexagons and triangles. As reported in twisted multilayer silicone [60] that quantum destructive interference in kagome geometry will lead to electron localization and flat bands, the kagome-like geometric features can be considered as a key role to understand the flat bands in our discovered P-$3m1$-Bi_{72}. Finally, we introduce kagome boundaries into supercells of various sizes, creating superperiodic systems to verify the sufficiency of kagome pattern-induced flat bands. The results in Fig. S7 show that flat bands are present across different system sizes [57], highlighting the strong correlation between the kagome pattern and flat bands.

Given the significant influence of SOC in the formation of flat bands, we have further investigated the spin texture properties of P-$3m1$-Bi_{72}. By comparing the spin vectors in plane and out of plane of the flat bands of P-$3m1$-Bi_{72} in momentum space, the BZ and high-symmetry points are illustrated in Fig. 4(d). As a result of the central symmetry present in the structure, all the energy bands are doubly degenerate, with the two components of the doubly degenerate bands exhibiting

opposite spin polarizations, similar to LaOBiS$_2$ [61]. For simplicity, our work focuses on presenting the spin structure of the highest valence band (VB1) as an example. In Fig. 4(a), the in-plane spin textures are depicted, with the background color indicating the magnitude. The black arrows represent the in-plane spin textures, and the orientation of the spin is plotted in the inset. Notably, the in-plane spin demonstrates twofold (180°) rotation symmetry and increases in magnitude as it moves away from Γ, reaching a peak at the M and $M-$ points. The magnitude of the out-of-plane spin is shown in Fig. 4(b), showing also twofold (180°) rotation symmetry within the BZ, with Γ exhibiting the maximum magnitude. In P-$3m1$-Bi$_{72}$, opposite spin orientations are observed near the $K+$ and $K-$ points. The spin orientation near $K+$ is achieved by rotating the spin orientation near $K-$ by 180° around the center of the BZ. This phenomenon is analogous to the counter-rotating vortices of the spin in the twisted homobilayer MoS$_2$ at the $K+$ and $K-$ points in the BZ [62]. In addition, the spin structures in the flat bands CB1 and CB3 still exhibit similar twofold rotation symmetry. A comparison reveals that both the in-plane and out-of-plane spin components of the highest valence band exhibit periodic changes in the Γ-M direction. Figure 4(c) illustrates the spin magnitude along the extension line of the Γ-M direction. It is evident that the in-plane spin reaches its maximum at point M and becomes zero at point Γ. The spin direction points towards the Γ-M direction. Conversely, the out-of-plane spin shows the opposite behavior, being maximum at point Γ and minimum at point M. This periodic variation of the spin textures has wide applications in the construction of polarized spin optoelectronic devices [63], such as optical analog of the Datta and Das spin transistor [64]. Overall, the spin textures exhibit a twofold rotation symmetry across the entire BZ, with the spin in VB1 vibrating periodically along the Γ-M direction. This phenomenon is a result of the specific polarization direction imposed by the crystal field and plays a crucial role in shaping the electron spin textures.

IV. CONCLUSIONS

In summary, a metastable configuration of 2D bismuthene (P-$3m1$-Bi$_{72}$) with multiple isolated flat bands near the Fermi level is identified through a high-throughput method. P-$3m1$-Bi$_{72}$ has a kagome-like boundary formed by consistently undulating Bi–Bi bonds (three pairs) between triangles and hexagons. The first-principles calculations confirms that P-$3m1$-Bi$_{72}$ is a dynamically and thermally stable semiconductor with three isolated flat bands throughout the entire BZ. These isolated flat bands can be well understood by the kagome-like distributions of charge density and the kagome-like boundary of atomic configuration. Their isolation and flatness are severely affected by the strength of SOC. The **k**-dependent spin texture of the flat bands in P-$3m1$-Bi$_{72}$ exhibits twofold rotation symmetry across the entire BZ and shows periodic variations along the Γ-M direction. This unique spin property has broad applications to construct spin-dependent optoelectronic devices. Our findings provide a candidate material for studying the properties of isolated flat bands in systems with strong SOC.

[1] J. Mao, S. P. Milovanović, M. Anđelković, X. Lai, Y. Cao, K. Watanabe, T. Taniguchi, L. Covaci, F. M. Peeters, A. K. Geim *et al.*, Evidence of flat bands and correlated states in buckled graphene superlattices, Nature (London). **584**, 215 (2020).

[2] O. Katz, G. Refael, and N. H. Lindner, Optically induced flat bands in twisted bilayer graphene, Phys. Rev. B **102**, 155123 (2020).

[3] T. Mizoguchi and M. Udagawa, Flat-band engineering in tight-binding models: Beyond the nearest-neighbor hopping, Phys. Rev. B **99**, 235118 (2019).

[4] S. M. Zhang and L. Jin, Flat band in two-dimensional non-Hermitian optical lattices, Phys. Rev. A **100**, 043808 (2019).

[5] S. Takayoshi, H. Katsura, N. Watanabe, and H. Aoki, Phase diagram and pair Tomonaga-Luttinger liquid in a Bose-Hubbard model with flat bands, Phys. Rev. A **88**, 063613 (2013).

[6] N. B. Kopnin, T. T. Heikkilä, and G. E. Volovik, High-temperature surface superconductivity in topological flat-band systems, Phys. Rev. B **83**, 220503(R) (2011).

[7] E. Tang and L. Fu, Strain-induced partially flat band, helical snake states and interface superconductivity in topological crystalline insulators, Nat. Phys. **10**, 964 (2014).

[8] C. Wu, D. Bergman, L. Balents, and S. Das Sarma, Flat bands and Wigner crystallization in the honeycomb optical lattice, Phys. Rev. Lett. **99**, 070401 (2007).

[9] Y. Chen, S. Xu, Y. Xie, C. Zhong, C. Wu, and S. B. Zhang, Ferromagnetism and Wigner crystallization in kagome graphene and related structures, Phys. Rev. B **98**, 035135 (2018).

[10] Y.-F. Zhao, R. Zhang, R. Mei, L.-J. Zhou, H. Yi, Y.-Q. Zhang, J. Yu, R. Xiao, K. Wang, N. Samarth *et al.*, Tuning the Chern number in quantum anomalous Hall insulators, Nature (London). **588**, 419 (2020).

[11] S. D. Huber and E. Altman, Bose condensation in flat bands, Phys. Rev. B **82**, 184502 (2010).

[12] M. Maksymenko, R. Moessner, and K. Shtengel, Persistence of the flat band in a kagome magnet with dipolar interactions, Phys. Rev. B **96**, 134411 (2017).

[13] Y. Cao, V. Fatemi, A. Demir, S. Fang, S. L. Tomarken, J. Y. Luo, J. D. Sanchez-Yamagishi, K. Watanabe, T. Taniguchi, E. Kaxiras *et al.*, Correlated insulator behaviour at half-filling in magic-angle graphene superlattices, Nature (London). **556**, 80 (2018).

[14] L. Feng, X. Lin, L. Meng, J.-C. Nie, J. Ni, and L. He, Flat bands near Fermi level of topological line defects on graphite, Appl. Phys. Lett. **101**, 113113 (2012).

[15] G. E. Volovik, Flat band in the core of topological defects: Bulk-vortex correspondence in topological superfluids with Fermi points, JETP Lett. **93**, 66 (2011).

[16] G.-B. Jo, J. Guzman, C. K. Thomas, P. Hosur, A. Vishwanath, and D. M. Stamper-Kurn, Ultracold atoms in a tunable optical kagome lattice, Phys. Rev. Lett. **108**, 045305 (2012).

[17] R. A. Vicencio, C. Cantillano, L. Morales-Inostroza, B. Real, C. Mejía-Cortés, S. Weimann, A. Szameit, and M. I. Molina, Observation of localized states in Lieb photonic lattices, Phys. Rev. Lett. **114**, 245503 (2015).

[18] H. Wang, B. Yang, W. Xu, Y. Fan, Q. Guo, Z. Zhu, and C. T. Chan, Highly degenerate photonic flat bands arising from complete graph configurations, Phys. Rev. A **100**, 043841 (2019).

[19] W. Han, K. Pi, K. M. McCreary, Y. Li, J. J. I. Wong, A. G. Swartz, and R. K. Kawakami, Tunneling spin injection into single layer graphene, Phys. Rev. Lett. **105**, 167202 (2010).

[20] W. Han, R. K. Kawakami, M. Gmitra, and J. Fabian, Graphene spintronics, Nat. Nanotechnol. **9**, 794 (2014).

[21] T. Liu and G. Vignale, Electric control of spin currents and spin-wave logic, Phys. Rev. Lett. **106**, 247203 (2011).

[22] H. Nakai and C. Hotta, Perfect flat band with chirality and charge ordering out of strong spin-orbit interaction, Nat. Commun. **13**, 579 (2022).

[23] G. Gligorić, A. Maluckov, L. Hadžievski, S. Flach, and B. A. Malomed, Nonlinear localized flat-band modes with spin-orbit coupling, Phys. Rev. B **94**, 144302 (2016).

[24] D.-S. Ma, Y. Xu, C. S. Chiu, N. Regnault, A. A. Houck, Z. Song, and B. A. Bernevig, Spin-orbit-induced topological flat bands in line and split graphs of bipartite lattices, Phys. Rev. Lett. **125**, 266403 (2020).

[25] M. Kang, S. Fang, L. Ye, H. C. Po, J. Denlinger, C. Jozwiak, A. Bostwick, E. Rotenberg, E. Kaxiras, J. G. Checkelsky *et al.*, Topological flat bands in frustrated kagome lattice CoSn, Nat. Commun. **11**, 4004 (2020).

[26] S.-S. Zhang, H. Ishizuka, H. Zhang, G. B. Halász, and C. D. Batista, Real-space Berry curvature of itinerant electron systems with spin-orbit interaction, Phys. Rev. B **101**, 024420 (2020).

[27] S. Zhang, M. Xie, F. Li, Z. Yan, Y. Li, E. Kan, W. Liu, Z. Chen, and H. Zeng, Semiconducting group 15 monolayers: A broad range of band gaps and high carrier mobilities, Angew. Chem. Int. Ed. **55**, 1666 (2015).

[28] E. Aktürk, O. Ü. Aktürk, and S. Ciraci, Single and bilayer bismuthene: Stability at high temperature and mechanical and electronic properties, Phys. Rev. B **94**, 014115 (2016).

[29] D.-C. Zhang, A.-X. Zhang, S.-D. Guo, and Y.-f. Duan, Thermoelectric properties of β-As, Sb and Bi monolayers, RSC Adv. **7**, 24537 (2017).

[30] F. Ersan, E. Aktürk, and S. Ciraci, Stable single-layer structure of group-V elements, Phys. Rev. B **94**, 245417 (2016).

[31] X. Liu, S. Zhang, S. Guo, B. Cai, S. A. Yang, F. Shan, M. Pumera, and H. Zeng, Advances of 2D bismuth in energy sciences, Chem. Soc. Rev. **49**, 263 (2020).

[32] H. L. Chia, N. M. Latiff, R. Gusmão, Z. Sofer, and M. Pumera, Cytotoxicity of shear exfoliated pnictogen (As, Sb, Bi) nanosheets, Chem. – Eur. J. **25**, 2242 (2019).

[33] K. Shen, H. Hua, Z. Liang, Y. Wang, H. Sun, J. Hu, H. Zhang, H. Li, Z. Jiang, H. Huang *et al.*, Epitaxial growth of free-standing bismuth film on graphene embedded with nontrivial properties, ACS Appl. Electron. Mater. **1**, 1817 (2019).

[34] P. J. Kowalczyk, O. Mahapatra, M. Le Ster, S. A. Brown, G. Bian, X. Wang, and T. C. Chiang, Single atomic layer allotrope of bismuth with rectangular symmetry, Phys. Rev. B **96**, 205434 (2017).

[35] S. Manipatruni, D. E. Nikonov, and I. A. Young, Beyond CMOS computing with spin and polarization, Nat. Phys. **14**, 338 (2018).

[36] J. C. R. Sánchez, L. Vila, G. Desfonds, S. Gambarelli, J. P. Attané, J. M. De Teresa, C. Magén, and A. Fert, Spin-to-charge conversion using Rashba coupling at the interface between non-magnetic materials, Nat. Commun. **4**, 2944 (2013).

[37] W. Ning, F. Kong, C. Xi, D. Graf, H. Du, Y. Han, J. Yang, K. Yang, M. Tian, and Y. Zhang, Evidence of topological two-dimensional metallic surface states in thin bismuth nanoribbons, ACS Nano. **8**, 7506 (2014).

[38] C. Xiao, F. Wang, S. A. Yang, Y. Lu, Y. Feng, and S. Zhang, Elemental ferroelectricity and antiferroelectricity in group-V monolayer, Adv. Funct. Mater. **28**, 1707383 (2018).

[39] J. Gou, H. Bai, X. Zhang, Y. L. Huang, S. Duan, A. Ariando, S. A. Yang, L. Chen, Y. Lu, and A. T. S. Wee, Two-dimensional ferroelectricity in a single-element bismuth monolayer, Nature (London). **617**, 67 (2023).

[40] Y. Zhang, C. Cui, C. He, T. Ouyang, J. Li, and C. Tang, Coexistence of out-of-plane and in-plane ferroelectricity in ultrathin elemental group-V nanotube arrays, Phys. Rev. B **108**, 245416 (2023).

[41] S. Zhong, X. Zhang, S. Liu, S. A. Yang, and Y. Lu, Giant and nonanalytic negative piezoelectric response in elemental group-Va ferroelectric monolayers, Phys. Rev. Lett. **131**, 136801 (2023).

[42] Z. Wang and S. Dong, Large in-plane negative piezoelectricity and giant nonlinear optical susceptibility in elementary ferroelectric monolayers, Phys. Rev. B **108**, 235423 (2023).

[43] H.-H. Song, W.-M. Wang, M. Chen, and Z.-M. Sheng, From linear to nonlinear Breit-Wheeler pair production in laser-solid interactions, Phys. Rev. E **109**, 035204 (2024).

[44] C. He, X. Shi, S. J. Clark, J. Li, C. J. Pickard, T. Ouyang, C. Zhang, C. Tang, and J. Zhong, Complex low energy tetrahedral polymorphs of group IV elements from first principles, Phys. Rev. Lett. **121**, 175701 (2018).

[45] X. Shi, C. He, C. J. Pickard, C. Tang, and J. Zhong, Stochastic generation of complex crystal structures combining group and graph theory with application to carbon, Phys. Rev. B **97**, 014104 (2018).

[46] Y. Liao, X. Shi, T. Ouyang, J. Li, C. Zhang, C. Tang, C. He, and J. Zhong, New two-dimensional wide band gap hydrocarbon insulator by hydrogenation of a biphenylene sheet, J. Phys. Chem. Lett. **12**, 8889 (2021).

[47] G. Kresse and J. Furthmüller, Efficient iterative schemes for ab initio total-energy calculations using a plane-wave basis set, Phys. Rev. B **54**, 11169 (1996).

[48] Z. Gong, X. Shi, J. Li, S. Li, C. He, T. Ouyang, C. Zhang, C. Tang, and J. Zhong, Theoretical prediction of low-energy Stone-Wales graphene with an intrinsic type-III Dirac cone, Phys. Rev. B **101**, 155427 (2020).

[49] X. Shi, S. Li, J. Li, T. Ouyang, C. Zhang, C. Tang, C. He, and J. Zhong, High-throughput screening of two-dimensional planar sp^2 carbon space associated with a labeled quotient graph, J. Phys. Chem. Lett. **12**, 11511 (2021).

[50] H. C. Yin, X. Shi, C. He, M. Martinez-Canales, J. Li, C. J. Pickard, C. Tang, T. Ouyang, C. Zhang, and J. Zhong, Stone-Wales graphene: A two-dimensional carbon semimetal with magic stability, Phys. Rev. B **99**, 041405(R) (2019).

[51] L. Kou, X. Tan, Y. Ma, H. Tahini, L. Zhou, Z. Sun, D. Aijun, C. Chen, and S. C. Smith, Tetragonal bismuth bilayer: A stable and robust quantum spin Hall insulator, 2D Mater. **2**, 045010 (2015).

[52] S. Zhang, S. Guo, Z. Chen, Y. Wang, H. Gao, J. Gómez-Herrero, P. Ares, F. Zamora, Z. Zhu, and H. Zeng, Recent progress in 2D group-VA semiconductors: From theory to experiment, Chem. Soc. Rev. **47**, 982 (2018).

[53] Y. Lu, W. Xu, M. Zeng, G. Yao, L. Shen, M. Yang, Z. Luo, F. Pan, K. Wu, T. Das *et al.*, Topological properties determined by atomic buckling in self-assembled ultrathin Bi(110), Nano Letters. **15**, 80 (2014).

[54] J. Heyd, J. E. Peralta, G. E. Scuseria, and R. L. Martin, Energy band gaps and lattice parameters evaluated with the Heyd-Scuseria-Ernzerhof screened hybrid functional, J. Chem. Phys. **123**, 174101 (2005).

[55] X.-A. Chen, S. Li, J. Li, C. He, T. Ouyang, C. Zhang, C. Tang, and J. Zhong, General and transferable tight binding model for two-dimensional bismuth allotropes, Phys. Scr. **98**, 055916 (2023).

[56] L. Su, S. Li, J. Li, C. He, X.-T. Zeng, X.-L. Sheng, T. Ouyang, Z. Chunxiao, C. Tang, and J. Zhong, $I4/mcm$-Si$_{48}$: An ideal topological nodal-line semimetal, ACS Materials Letters. **4**, 1726 (2022).

[57] See Supplemental Material at http://link.aps.org/supplemental/10.1103/PhysRevB.110.115115 for supplemental tables, figures, and the optimized crystal structures of the 57 bismuth allotropes with flat bands.

[58] Z. Zhu and D. Tománek, Semiconducting layered blue phosphorus: A computational study, Phys. Rev. Lett. **112**, 176802 (2014).

[59] H. Liu, S. Meng, and F. Liu, Screening two-dimensional materials with topological flat bands, Phys. Rev. Mater. **5**, 084203 (2021).

[60] Z. Li, J. Zhuang, L. Wang, H. Feng, Q. Gao, X. Xu, W. Hao, X. Wang, C. Zhang, K. Wu *et al.*, Realization of flat band with possible nontrivial topology in electronic Kagome lattice, Sci. Adv. **4**, eaau4511 (2018).

[61] X. Zhang, Q. Liu, J.-W. Luo, A. J. Freeman, and A. Zunger, Hidden spin polarization in inversion-symmetric bulk crystals, Nat. Phys. **10**, 387 (2014).

[62] B. T. Zhou, S. Egan, and M. Franz, Moiré flat Chern bands and correlated quantum anomalous Hall states generated by spin-orbit couplings in twisted homobilayer MoS$_2$, Phys. Rev. Res. **4**, L012032 (2022).

[63] T. C. H. Liew, I. A. Shelykh, and G. Malpuech, Polaritonic devices, Physica E (Amsterdam, Neth.) **43**, 1543 (2011).

[64] R. Johne, I. A. Shelykh, D. D. Solnyshkov, and G. Malpuech, Polaritonic analogue of Datta and Das spin transistor, Phys. Rev. B **81**, 125327 (2010).